

Multifunctionality of Nanoengineered Self-Sensing Lattices Enabled by Additive Manufacturing

Jabir Ubaid, Johannes Schneider, Vikram S. Deshpande, Brian L. Wardle, and Shanmugam Kumar*

Lightweight cellular materials are engineered to enhance performance attributes such as energy absorption, specific stiffness, negative Poisson's ratio, negative thermal expansion coefficient, etc. However, self-sensing functionality of such architected materials is seldom explored. Herein, a combined experimental and numerical study on additive manufacturing (AM)-enabled self-sensing cellular composites processed via fused filament fabrication, utilizing in-house engineered multiwall carbon nanotube (MWCNT)/polypropylene random copolymer (PPR) filament feedstocks, is reported. The tunable self-sensing and enhanced mechanical performance of PPR/MWCNT lattices are experimentally demonstrated by varying their architectural parameters in addition to the MWCNT content. The lattices reveal strain and damage sensitivity gauge factors of 12 and 1.2, respectively, comparable to bulk materials' commercial gauge factors. Furthermore, self-sensing lattices exhibit 200%, 155%, 153%, and 137% increase in stiffness, energy absorption capacity (as high as 4.7 MJ m^{-3}), specific energy absorption (20.5 J g^{-1}), and energy absorption efficiency (90%), respectively, compared with their non-reinforced counterparts. The tunable multifunctional performance of AM-enabled cellular composites demonstrated here provides guidelines for the design and development of composite lattices with advantaged structural and functional properties for an array of applications such as patient-specific biomedical devices capable of measuring comfort in prosthetics.

length scales. Periodic cellular solids, usually referred to as lattices, possess a desired combination of properties such as strength and toughness and are widely used in aerospace, automotive,^[6] biomedical,^[7] energy storage,^[8] and construction sectors,^[9] as they outperform foams.^[10] In the pursuit of lightweight engineering, there is a constant urge for developing low-density lattices with excellent mass-specific properties.^[11,5a,5b] An important aspect of such lattices is that their properties can be tuned by carefully controlling the architectural parameters such as unit-cell geometry, unit-cell size, and ligament size^[5a,11b,12] for a given choice of constituent material(s). Custom-tailored materials for specific application requirements are common, and the emergence of additive manufacturing (AM) technologies enables fabrication of cellular structures with intricate 3D architectures at different length scales from a variety of materials such as metals, polymers, ceramics, and composites.^[11c,12b,13] AM is particularly suitable for the fabrication and design of complex 3D cellular structures as it eliminates the need for expensive tooling and dies.

1. Introduction

Cellular forms are omnipresent in nature and are found in wood,^[1] cork,^[2] beehives, sponge,^[3] and bone^[4] where the performance or function is governed by the intricate arrangement of matter and pores that lead to excellent mechanical and/or functional properties.^[5] Nature-inspired cellular materials have a periodic or stochastic arrangement of building blocks at different

Self-sensing lattices are capable of monitoring environments in addition to performing the intended primary function(s) in service. Such a sensing ability is useful for monitoring the in situ deformation state and/or damage state of the structure.^[14] For instance, these self-sensing lattices can also be used as smart rehabilitation assistive devices, and material architecture for robotics where sensing, control, and actuation are essential for increasing the efficiency of the robot's function.^[15] Self-sensing

J. Ubaid, J. Schneider, S. Kumar
James Watt School of Engineering
University of Glasgow
Glasgow G12 8LT, UK
E-mail: s.kumar@eng.oxon.org

 The ORCID identification number(s) for the author(s) of this article can be found under <https://doi.org/10.1002/adem.202200194>.

© 2022 The Authors. Advanced Engineering Materials published by Wiley-VCH GmbH. This is an open access article under the terms of the Creative Commons Attribution License, which permits use, distribution and reproduction in any medium, provided the original work is properly cited.

DOI: 10.1002/adem.202200194

V. S. Deshpande
Department of Engineering
University of Cambridge
Trumpington Street, Cambridge CB2 1PZ, UK

B. L. Wardle
Department of Aeronautics and Astronautics
Massachusetts Institute of Technology
Cambridge, MA 02139, USA

B. L. Wardle
Department of Mechanical Engineering
Massachusetts Institute of Technology
Cambridge, MA 02139, USA

can be engineered either by embedding sensing elements into the material or by creating multifunctional materials, which exhibit intrinsic sensing ability in response to external stimuli.^[14d,16] In this study, we focus on the latter approach and demonstrate the self-sensing performance of AM-enabled 3D cellular composites.^[17] Such multifunctional composites enable transduction of mechanical stimuli into electric signals based on piezoresistive, piezocapacitive, piezoelectric, supercapacitive ionic, and triboelectric mechanisms.^[14e,16e,16l,18] If sufficient amount of electrically conductive fillers is incorporated into a nonconductive matrix, conductive fillers form an electrically percolated conductive network within the matrix.^[19] The resulting electrically conductive composites exhibit a change in electrical resistance under external stimuli such as strain, referred to as piezoresistivity.^[20] The piezoresistive behavior of such smart composites can be leveraged to monitor the in situ environment. For example, Yang et al.^[21] developed 3D-printed lightweight smart armor with aligned graphene nano-platelets that can sense damage via its piezoresistive behavior.

Polypropylene (PP) and its composites are widely used for various engineering applications such as automotive, aerospace, marine, biomedical, piping, and construction industry due to their favorable properties such as excellent strength to weight ratio, high-energy absorption, corrosion resistance, environmental stress-cracking resistance, less water absorption, and weldability.^[22] Cellular structures made of PP and its composites are used as core of sandwich structures, prosthetic mesh for biomedical applications, and energy-absorbing foams in automotive bumpers, seating, and door panels.^[23] They can be potentially used in areas where spatially varying properties are desired, for instance, custom-made orthoses for scoliosis.^[23c,24] Cellular PP structures nano-engineered with electrically conductive fillers such as graphene,^[25] MXene,^[16g] and metallic nanoparticles (such as gold and silver, etc.) could be useful for a multitude of applications. For instance, detection of damage initiation in cores of sandwich structures used in aerospace industry is of utmost importance to avoid catastrophic failure of the structure.^[26]

As the fabrication of cellular structures with intricate architectures is either cumbersome or impossible with traditional manufacturing methods, fused filament fabrication (FFF) AM was used to realize lattice structures, utilizing in-house nano-engineered polypropylene random copolymer/multiwall carbon nanotube (PPR/MWCNT) composite filaments. A range of lattice structures with varying constituent material (MWCNT content in the PPR matrix) and also architectural parameters (unit-cell geometry and the relative density) were realized. Lattices of three different architectures, namely body-centered cubic (BCC) plate-lattice, open-cell Kelvin foam, and gyroid-lattice with varying relative density ($\bar{\rho} = \rho/\rho_s$, where ρ is the density of cellular structure and ρ_s is the density of constituent solid material), were additively manufactured at mesoscale. Each lattice has $2 \times 2 \times 2$ unit cells (see **Figure 1**). BCC plate-lattice is a closed-cell cellular structure comprising plates or shells^[11e] placed in closest packed planes as in BCC crystals. Closed-cell structures are found to be capable of achieving close to Hashin–Shtrikman upper bounds on isotropic elastic stiffness due to the material constraints in two directions.^[11b] Open-cell Kelvin foam is a bending-dominated

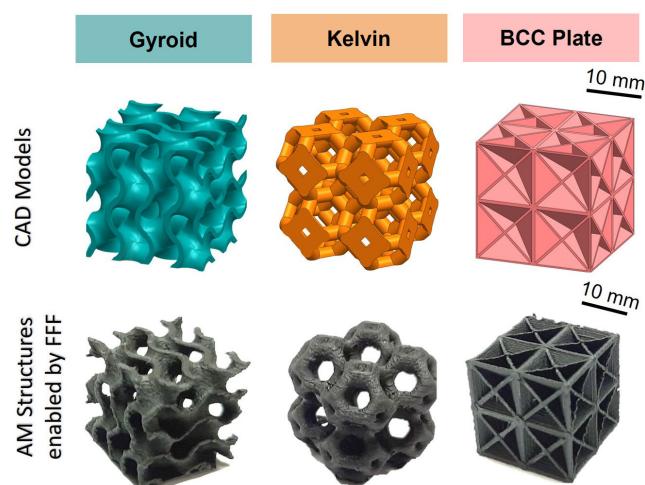


Figure 1. Design and fabrication of polypropylene random copolymer/multiwall carbon nanotube (PPR/MWCNT) cellular structures: CAD models and images of additively manufactured PPR/MWCNT lattices with 6 wt% carbon nanotube (CNT) and 30% relative density.

structure composed of struts. It comprises tetrakaidehedral unit-cells whose faces contain 8 hexagons and 6 squares.^[27] The sheet-based gyroid-lattices belong to the class of cellular structures that are made from triply periodic minimal surface geometries and are found to exhibit stretch-dominated deformation behavior, enabling them to outperform most of the strut-based lattices in terms of mechanical performance. We engineer piezoresistive PPR/MWCNT nanocomposites incorporating MWCNTs into PPR matrix to monitor the in situ strain state and/or damage state of lattice structures. Both self-sensing and mechanical performance of FFF AM-enabled PPR/MWCNT composite lattice structures under quasi-static compressive loading are demonstrated. To the best of authors' knowledge, studies on AM-enabled self-sensing cellular structures have not thus far been reported in the literature. The results indicate that our AM-enabled 3D lattices exhibit both piezoresistive sensitivity and energy absorption characteristics superior to those of extant works.

2. Experimental Section

2.1. Materials

The lattice structures explored in this study were additively manufactured using multiwall carbon nanotube (MWCNT) incorporated polypropylene random (PPR) copolymer filaments. PPR, which forms the matrix phase in the composite, was provided by Borouge Pte, UAE, in pellet form. In contrast to PP, the chosen PPR offers enhanced processability, improved temperature resistance, better product consistency, and better impact strength. MWCNTs grown by chemical vapor deposition (CVD) technique were supplied by Applied Nanostructured Solutions LLC, USA. Detailed characterization of MWCNTs were performed in previous studies of our group.^[14d,28] The surface morphology analysis of MWCNTs using scanning electron

microscopy (SEM) revealed that the MWCNTs have an average diameter of 10–12 nm and an aspect ratio >3000. The multi-walled ($\alpha - \gamma$ walls on average) structure of the carbon nanotubes (CNTs) was confirmed from the Raman spectroscopy analysis.^[14d,28] PPR was found to have a melting temperature of 147 °C, a crystalline temperature of 112 °C, and a crystallinity of 30 wt% after FFF printing (see Section S1 and Figure S1, Supporting Information).

2.2. Filament Fabrication and Additive Manufacturing of 3D Lattices

MWCNT-engineered PPR filaments were fabricated by a melt blending technique using a corotating twin-screw extruder (Coperion ZSK 18) (see Section S2 and Figure S2, Supporting Information). Vacuum-dried PPR and MWCNTs were used for the filament fabrication. Filaments of 1.75 mm diameter were made in different batches with different weight fractions (0, 2, 4, 6, and 8 wt%) of MWCNT in the PPR matrix. The thermoplastic filaments thus developed are used as feedstock in FFF AM to fabricate lattice geometries. The PPR/MWCNT lattices with different architectures (see Figure 1) and relative densities (20% and 30%) were fabricated using Creator Pro 3D printer from Flashforge, USA. The computer-aided design (CAD) models of bulk and cellular structures were prepared using the CAD program SolidWorks (Dassault Systèmes SolidWorks Corp., USA). The slicing software Simplify3D was used to convert the CAD models into printable files. The filament was heated and dispensed through the nozzle on to the print bed to build the geometry layer by layer. The same printing/process parameters such as nozzle temperature (230 °C), bed temperature (115 °C), layer height (120 μm), and infill density (100%) were consistently used for all the prints.

2.3. Characterization

SEM was used to characterize the surface morphology of the additively manufactured PPR/MWCNT cellular lattices. Gold-coated (coating thickness of ≈ 10 nm) samples were analyzed using Nova Nano SEM 50 series (FEI, USA) with a working distance of 5 mm. DC electrical conductivity of additively manufactured bulk samples were measured by four-probe conductivity measurement method (Van der Pauw method) using LakeShore 7607 (LakeShore Cryotronics, USA) to obtain an average (nondirectional) conductivity measurement free of contact resistance effects. To minimize the contact resistance between the electrodes and the sample, silver paste was applied on the sample surface at the contact points. The mechanical performance of the additively manufactured bulk samples under quasi-static monotonic tension and compression, as well as the mechanical performance of cellular structures under quasi-static monotonic compressive load, was experimentally evaluated using an Instron 5969 universal testing machine fitted with a 50 kN load cell. The testing system had a force measurement accuracy of $\pm 0.5\%$ of the reading up to 0.2 kN, displacement accuracy of ± 0.01 mm or 0.05% of displacement (whichever is greater), and a position control resolution of 27 nm. Tensile and compressive tests were performed at a constant strain rate

of $16\% \text{ min}^{-1}$. The piezoresistive performance was evaluated during the mechanical testing by measuring the resistance of the samples using DMM 4050 Multimeter (Tektronix, USA). For the tensile tests, the electrodes of the multimeter were connected to the samples at the ends of the gauge length using a conductive epoxy. For compression tests, electrodes were connected to copper foils, which were pasted using regular tape to the compression fixtures so that the samples were pressed against the copper foils during compression tests. Each sample was tested at least three times to confirm the repeatability of the measurements. Videos of the cellular structures during compression loading were captured using a 25 MP camera.

2.4. Finite Element Analysis

For an in-depth understanding of the deformation modes, stress distributions and load-resisting mechanisms of different cellular structures, finite element (FE) simulations were performed using ABAQUS 2019 (Dassault Systèmes Simulia Corp., USA). The lattices were modeled using C3D10M (a 10-node-modified quadratic tetrahedron) elements with an average mesh size of 0.09 mm for the different architectures considered. The top and bottom compression platens of the compression test fixture were modeled as discrete rigid shells, and the cellular structure model was placed between the rigid surfaces. The bottom rigid surface was fixed, and the top rigid surface was given a downward displacement in the vertical direction to compress the samples as in the experiments. General contact was applied between all elements in the model by choosing hard contact for the normal contact behavior and frictional sliding with a coefficient of friction of 0.2 for the tangential contact behavior. The linear-elastic material model was calibrated with the measured stress–strain response of PPR/MWCNT composite specimens. The constitutive parameters were summarized in Table S1, Supporting Information, with a Poisson's ratio of 0.4, and a density of 0.94 g cm^{-3} were used for the FE analysis.

3. Results and Discussion

The mechanical and piezoresistive properties of the lattice parent materials are described, leading to the discussion of the mechanical and self-sensing performance of the architected lattice composites.

3.1. Piezoresistive and Mechanical Performance of Parent Composites

The isotropic electrical conductivity of printed PPR/CNT composites with varying CNT content is measured via 4-point probe method and plotted in Figure S3, Supporting Information. Many orders of electrical conductivity increase is observed as the CNT content increases from 0 to 8 wt%. The percolation threshold—a critical filler content at which the conductive network fully forms—is evaluated to be 1.4 wt%. PPR/CNT composite samples with 0, 4, and 6 wt% of CNT are produced by FFF AM and designated as PPR/CNT-0, PPR/CNT-4, and PPR/CNT-6, respectively. Mechanical tests together with piezoresistivity measurements were carried out on PPR/CNT composite bulk

samples produced by FFF AM (dog-bone tensile samples printed in 0° and 90° print-orientations are tested). Figure S4 and S6a, Supporting Information, show the stress–strain response of bulk PPR/CNT samples with varying CNT content under quasi-static tension and compression and the results are summarized in Table S1 and S2, Supporting Information, respectively. For 0° samples, the beads are parallel to the loading direction and for 90° samples, the print beads are perpendicular to the loading direction. Tensile tests on bulk samples reveal that an increase in CNT content in the PPR leads to a stiffer, stronger, and more brittle response of the composite. The increasing stiffness and strength of PPR/CNT composites with increase in CNT content is attributed to both the reinforcement effect of CNTs and the increased crystallinity of PPR due to the addition of CNTs (see Table S4 and S5, Supporting Information). The loss of strain tolerance of PPR/CNT composite at higher CNT content could be ascribed to the reduced mobility of the polymer chains due to the interaction of CNTs with the PPR matrix. Furthermore, a clear difference in performance can be seen between samples with different print orientations. Samples with 0° print orientation show higher tensile modulus, yield strength, tensile strength, and modulus of toughness compared to the samples with 90° print orientation, evidencing that the tensile mechanical properties are primarily governed by the orientation of beads with respect to loading direction, usually attributed to the quality of interfacial bonding and porosity between beads. Compression samples were built in 90° print orientation and their test results reveal that under compression PPR/CNT composites retain mechanical compliance with increase in CNT content (see Figure S6a, Supporting Information).

If the CNT content suffices to form an electrical percolation in the PPR matrix, the PPR/CNT composite becomes electrically conductive. The piezoresistive response of such electrically conductive PPR/CNT composites with varying CNT content under tension and compression are shown in Figure S5a–b (for 0° and 90° print orientations, under tension) and S6b, Supporting Information, (for 0° print orientation, under compression), respectively. The electrical resistance of PPR/CNT composites increases under tension with the limits of normalized change in resistance being 0 and ∞ , that is, $\Delta R/R_0 = [0, \infty]$, where $\Delta R = (R - R_0)$ is the change in resistance, R is the resistance of the samples under applied tensile strain ϵ , and R_0 is the initial resistance of the samples under no-load condition. In contrast, the resistance of the PPR/CNT composites decreases under compressive strain ϵ (also taken positive) with limits being 0 and -1 , that is, $-\Delta R/R_0 = [0, 1]$. The PPR/CNT composites under tension exhibit a maximum $\Delta R/R_0 = 260$ and 3.5 for the 0° and 90° print orientations, respectively, giving a resistance anisotropy ratio close to 75. The 0° PPR/CNT compression samples show a vanishingly small resistance ($-\Delta R/R_0 \approx 1$) at around $\epsilon = 40\%$. The strain sensitivities—the initial slope of normalized change in resistance versus strain curve of the samples—were quantified via a gauge factor ($k_s = \frac{1}{R_0} \frac{\Delta R}{\Delta \epsilon}$) and are summarized in Table S3, Supporting Information. The PPR/CNT composite with 4 wt% CNT was found to exhibit the highest initial gauge factor (corresponding to the elastic regime) both under tension and compression. A further increase in CNT wt% showed a reduction in the gauge

factor, as expected, due to the increased number of conduction channels. The PPR/CNT composites under tension exhibit a positive change in normalized change in resistance through mechanisms such as tunneling, changes in contact resistance between CNTs and destruction of conductive networks.^[29] The compression samples, as expected, show a decrease in normalized change in resistance due to percolation of conductive networks. The higher strain sensitivity of the samples comprising lower CNT content could be due to a fewer conductive paths compared to samples with higher CNT content, which leads to a higher change in resistance ($\Delta R/R_0$) under applied strain. Similar to mechanical behavior, piezoresistive response is also found to be influenced by the print orientation: 0° samples are found to show a higher gauge factor compared to samples with 90° print orientation. The print orientation governs the distribution and orientation of CNTs within the PPR matrix as well as inter-bead and intra-bead defect structure, influencing the piezoresistive behavior of PPR/MWCNT composites.

3.2. Performance of Cellular Composite Structures

PPR/CNT composite cellular structures of $2 \times 2 \times 2$ unit cells with varying CNT content and relative density were realized via FFF AM. Figure 1 shows the images of CAD models and AM-enabled cellular structures of three different architectures: BCC plate–lattice, Kelvin foam, and Gyroid–lattice. Cryogenic fracture tests of the samples were performed and the SEM images of the fractured surface of PPR/CNT-0 and PPR/CNT-6 samples are shown in Figure 2. The presence and uniform dispersion of CNTs in the PPR matrix can be seen in the SEM image of PPR/CNT-6 sample.

3.3. Piezoresistive Performance

PPR/MWCNT composite cellular structures of varying CNT content (0, 4, and 6 wt%) and relative density (20% and 30%) are tested under quasi-static compressive loading (and the corresponding compressive strain ϵ is taken as positive). As the PPR/MWCNT bulk composites are electrically conductive and show piezoresistive behavior, the changes in electrical resistance values of cellular structures of PPR/CNT-4 and PPR/CNT-6 were recorded during the quasi-static compression tests to assess their piezoresistive behavior. The piezoresistive response and the corresponding stress–strain behavior of different architectures with different relative densities are shown in Figure 3a–f, respectively. All the cellular structures show a decrease in electrical resistance as the applied compressive stress/strain increases, as expected. The initial piezoresistive response of all the three architectures is nearly linear (corresponding to linear–elastic deformation of the lattices), which is primarily attributed to the decrease in electrical resistance of the cell wall material due to percolation of conductive networks within the cell walls/ligaments via increase in number of contacts between CNTs and/or decrease in tunneling resistance. The initial linear piezoresistive response is followed by a reduction in the slope of the response, corresponding to plateau region of stress–strain response where yielding and progressive wrinkling of the cell walls govern the piezoresistance. In the third stage, an increase in the slope of $-\Delta R/R_0$ versus ϵ curve is

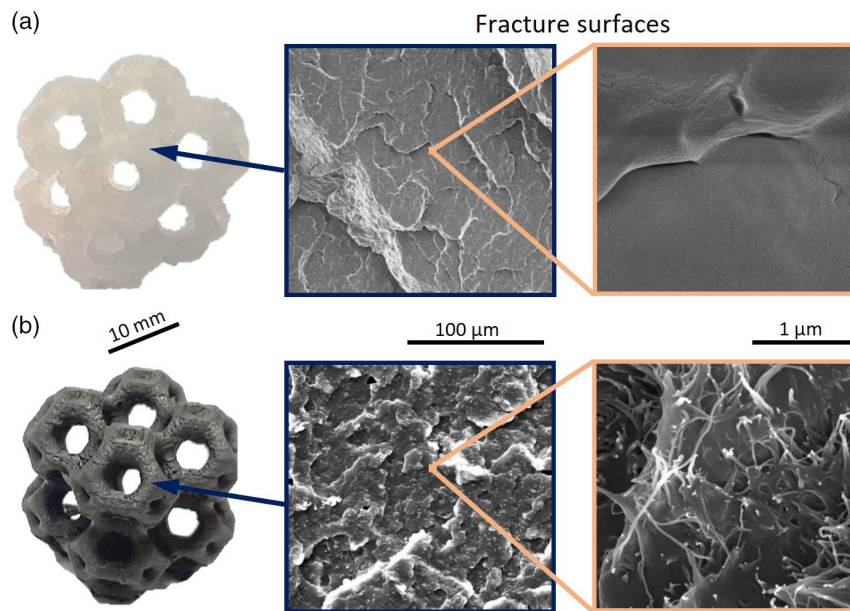


Figure 2. Additively manufactured cellular structures with 30% relative density (Kelvin foam): a) PPR/CNT-0 (neat) and b) PPR/CNT-6 show the surface morphology of cryogenically hand-fractured cross sections.

observed at the onset strain of densification where cell walls come into contact with each other (beginning of percolation of contacts between cell walls/ligaments), forming more conductive paths within the lattice. With further increase in compressive loading, the percolation of these lattice-level contacts grows, causing a steep increase in the slope of the $-\Delta R/R_0$ versus ϵ until the lattice is (nearly) completely compacted; the strain reaches a complete densification strain (the critical strain at which the cell walls jam together), and the resistance of the structure becomes vanishingly small, that is, $\Delta R/R_0 \approx -1$ for the BCC plate-lattice. The evolution of piezoresistance in the densification regime, in addition to the inelastic processes such as the plasticity and damage, is primarily governed by the percolation of contacts between cell walls. Similarly, the gyroid-lattice attain near-zero electrical resistance, $\Delta R/R_0 \approx -0.9$, although the Kelvin foam still exhibits 15% of its initial resistance around full densification, that is, $\Delta R/R_0 \approx -0.85$. The piezoresistive behavior ($-\Delta R/R_0$ vs ϵ) of different PPR/CNT cellular composite structures can be approximated by the Michaelis–Menten equation^[30] given by

$$\frac{-\Delta R}{R_0} = \frac{a\epsilon}{(b + \epsilon)} \quad (1)$$

Fitting parameters a and b for different architectures with corresponding relative density and CNT content are summarized in **Table 1** and the fit curves are compared with experimental curves in Figure S7, Supporting Information. Value of a is more than 1 only for 6 wt% CNT loaded, 30% relative density Kelvin-lattice. $a > 1$ signifies faster damage progression within the lattice under compression. In general, higher values of a indicate higher relative changes in resistance for a specified strain.

The stress–strain response of all the printed lattice structures exhibits typical behavior of cellular structures, comprising an

initial linear–elastic response followed by a plateau with small fluctuations in stress values (due to progressive wrinkling and yielding of cell walls/ligaments) and the densification regime where the contacts between cell walls/ligaments begin and proliferate. Compared to Kelvin and gyroid cellular structures, BCC plate-lattices are more stretching dominated. The drop in load and fluctuation of load in BCC structures could be due to the buckling of walls after contraction as the thickness of wall in BCC are lower compared to thickness of sheets in gyroid and diameter of struts in Kelvin structures. **Figure 4, 5** show optical images of the lattices (PPR/CNT-0, and PPR/CNT-6 with a relative density of 30%) at different strain levels under quasi-static compression (see the video SV1, Supporting Information, for synchronized mechanical and piezoresistive response with the deformation of neat and nanoengineered cellular structures). Deformation maps and the video SV1 in Supporting Information, indicate no macroscopic failure for any of the structures until near-full densification via a ductile-like behavior (see Figure 3d–f). The absence of macroscopic failure and the ductile-like behavior of the cellular structures made of stronger and stiffer nanocomposites (strength and stiffness of PPR/CNT bulk samples increases with increasing CNT content) results in enhanced mechanical performance of the PPR/CNT cellular structures with higher CNT content than those with lower or no CNT content.

The instantaneous slope of $\Delta R/R_0$ versus ϵ curve is called as instantaneous gauge factor, k , and is given by

$$k \stackrel{\text{def}}{=} \frac{1}{R_0} \left| \frac{dR}{d\epsilon} \right| \quad (2)$$

The instantaneous gauge factor, k , over the entire strain range for all three PPR/CNT lattices with different CNT contents and

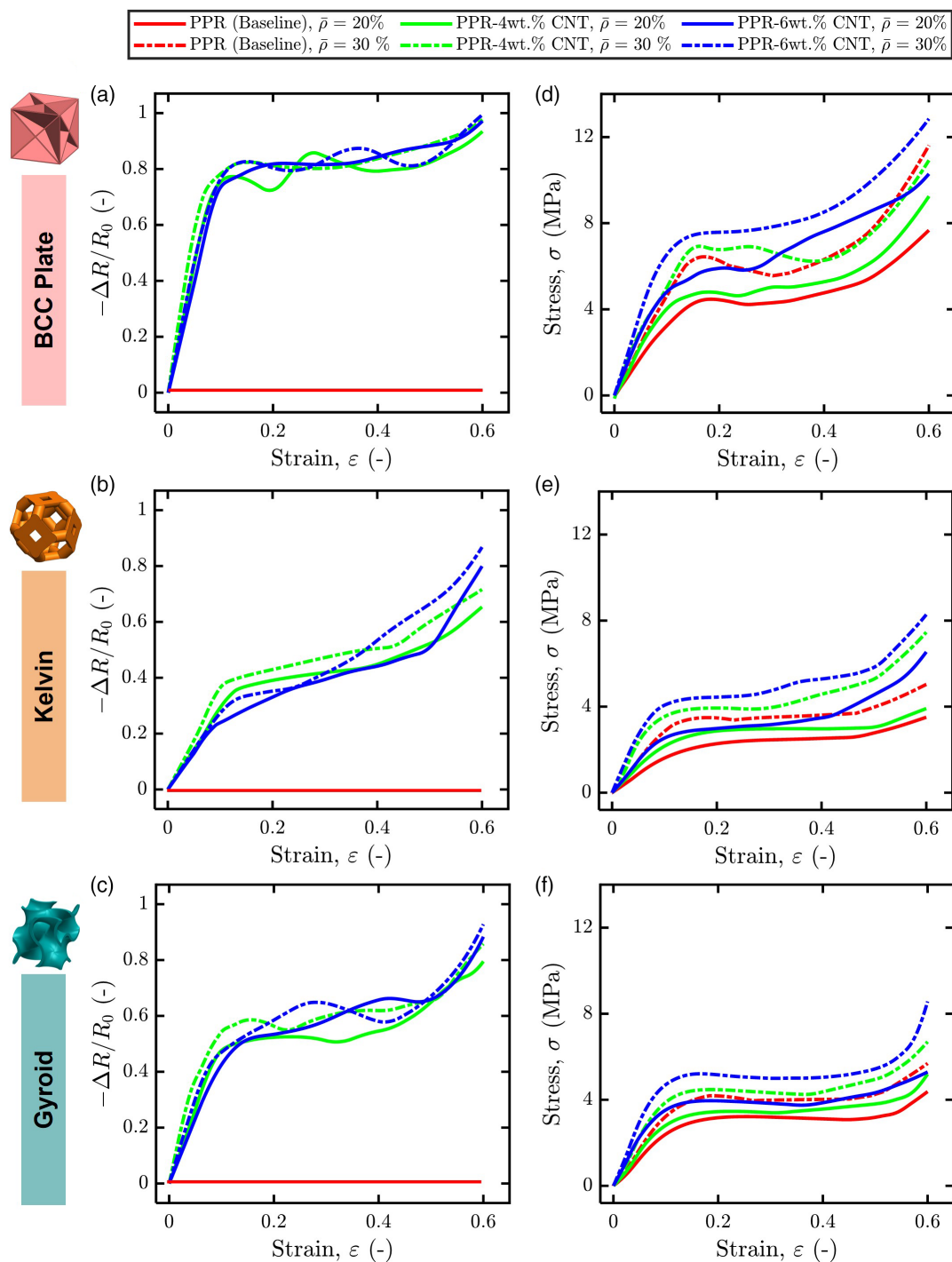


Figure 3. Representative piezoresistive and mechanical response of PPR/CNT cellular structures with different relative densities and CNT loadings under compression: a–c) piezoresistive response of different lattice structures. d–f) Stress–strain response of different lattice structures.

relative densities is shown in Figure S8, Supporting Information. It shows the k until critical densification strain at which the lattices become nearly fully conductive ($\Delta R/R_0 \approx -1$). Variation of k versus strain shows a nearly constant k in the beginning (corresponding to the linear–elastic response of the lattice) indicating the sensitivity of the structure to elastic

deformation, and is governed by the creation of additional conductive networks within the cell walls/ligaments. This leads to a decrease in contact resistance between CNTs and tunneling as observed for bulk samples under compression (see Figure S6b, Supporting Information). This regime is followed by a drop in k that corresponds to the beginning of inelastic

Table 1. Estimated fitting parameters for Michaelis–Menten equation given by $\frac{\Delta R}{R_0} = \frac{a\varepsilon}{(b+\varepsilon)}$.

Unit-cell architecture	CNT content [wt%]	Relative density [%]	a (–)	b (–)
BCC plate	4	20	0.9247	0.0409
		30	0.9253	0.0294
	6	20	0.9896	0.0531
		30	0.9565	0.0407
Kelvin	4	20	0.6017	0.118
		30	0.6540	0.1038
	6	20	0.6697	0.1996
		30	1.0069	0.3522
Gyroid	4	20	0.6425	0.0537
		30	0.6887	0.0394
	6	20	0.8039	0.1003
		30	0.7267	0.0585

response (plateau region in the stress–strain response, see Figure 3d–f). The morphology of conductive network corresponding to plateau region in the stress–strain curve is severely

affected by the inelastic processes such as the plasticity and microscopic damage of the cell walls/ligaments, resulting in lower values of k . However, around the onset strain of densification where percolation of contacts between cell walls/ligaments begins, k starts increasing. Higher value of k in the densification regime indicates faster percolation of contacts between cell walls/ligaments. k in the densification regime is of course governed by the percolation of contacts between cell walls in addition to inelastic processes such as the plasticity and damage of the cell walls/ligaments.

Strain sensitivity of the cellular structures to applied strain is measured by the gauge factor—the slope of $-\Delta R/R_0$ versus ε curve in the elastic regime, given by

$$k_s = \frac{1}{R_0} \left| \frac{\Delta R}{\Delta \varepsilon} \right| \quad (3)$$

where ΔR is the change in resistance over an applied compressive strain range $\Delta \varepsilon$ in the elastic loading branch. The strain sensitivity, k_s , of the lattices evaluated in the linear piezoresistive regime is plotted in Figure 6a–c and is summarized in Table 2. Note that k_s changes with architecture, relative density, and CNT content as expected. For a given strain, higher value of k_s indicates that the structure under compression is more sensitive to

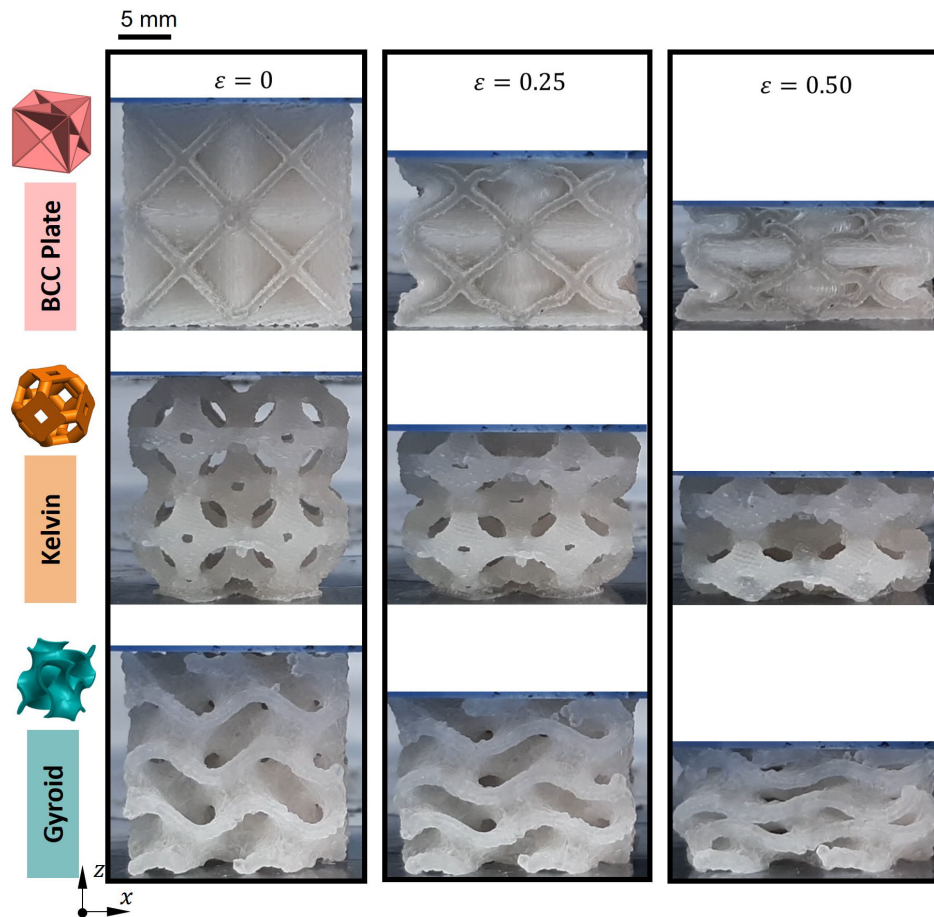


Figure 4. Optical images of PPR/CNT-0 (Baseline) cellular structures with a relative density of 30% show the deformation maps at different stages of compressive loading.

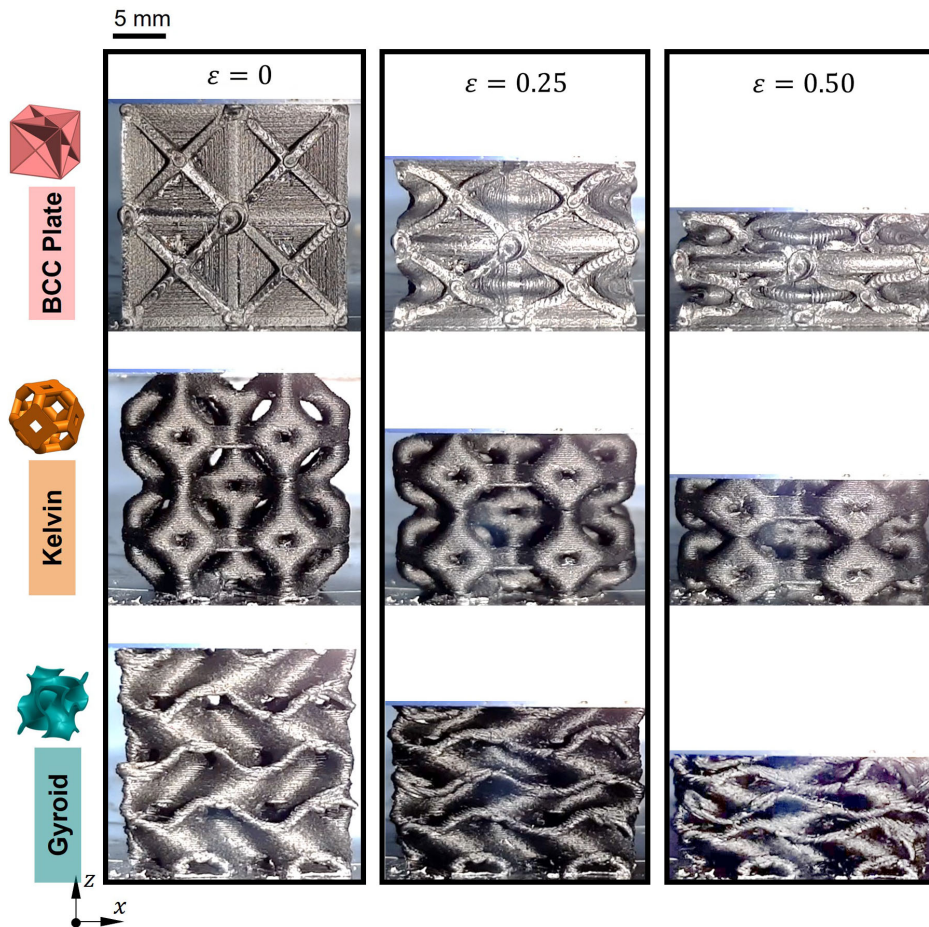


Figure 5. Optical images of PPR/CNT-6 cellular composites with a relative density of 30% show the deformation maps at different stages of compressive loading (to compare with baseline images in Figure 4).

elastic deformation. Lattices of PPR/CNT-4 show higher k_s compared to PPR/CNT-6, a trend similar to that observed in bulk samples (see discussion in Supporting Information Section S3 and Figure S5 and S6b, Supporting Information). PPR/CNTs with lower CNT loading (at or slightly above the percolation threshold) are expected to show a higher change in resistance with strain due to lesser number of contact junctions between CNTs compared to PPR/CNT composites with higher content of CNTs. From Table 2 and Figure 6, it can be inferred that the strain sensitivity reduces as the CNT content increases. A similar trend is observed for bulk samples (Figure S5 and S6b, Supporting Information). Generally, samples with lower CNT content shows higher sensitivity. This is due to a smaller number of conductive paths within the composite with lower CNT content, and therefore, change in resistance is relatively large to small, applied strain. In case of composites with higher CNT content, denser network of CNTs is formed and change in resistance is lower to applied strain.^[31] In addition, k_s of lattices increases as the relative density is increased from 20% to 30%. This could be due to the more stretching-dominated behavior of structures at higher relative densities as the thickness of walls/ligaments are higher and resist bending compared to samples of

lower relative density. A clear distinction in the strain sensitivity k_s is observed for different architectures. Higher strain sensitivity ($k_s = 8 - 12.2$) is noted for BCC plate-lattices whereas the lowest k_s values in a range of 2.6–3.5 are observed for Kelvin foams. Thus, the k_s of lattices of different architectures follows a trend similar to the mechanical performance. The difference in the piezoresistive response between different architectures can be attributed to their distinct deformation mechanisms/modes. Kelvin foams are bending-dominated structures whose members are subjected to more bending compared to BCC and gyroid lattices. Bending of cell walls/ligaments results in cell walls/ligaments being subjected to tensile stresses (or strains) and compressive stresses (or strains) in different regions of cell walls/ligaments. In the regions of tensile stresses (or strains), a local increase in the electrical resistance is expected as observed for bulk samples under tension (see Figure S5a,b, Supporting Information). In contrast, a local decrease in electrical resistance is expected in regions of compressive stresses within cell walls as observed for bulk samples under compression (see Figure S6b, Supporting Information). The net effect of bending, therefore, is not expected to cause a significant change in electrical resistance of structures such as Kelvin foam whose ligaments

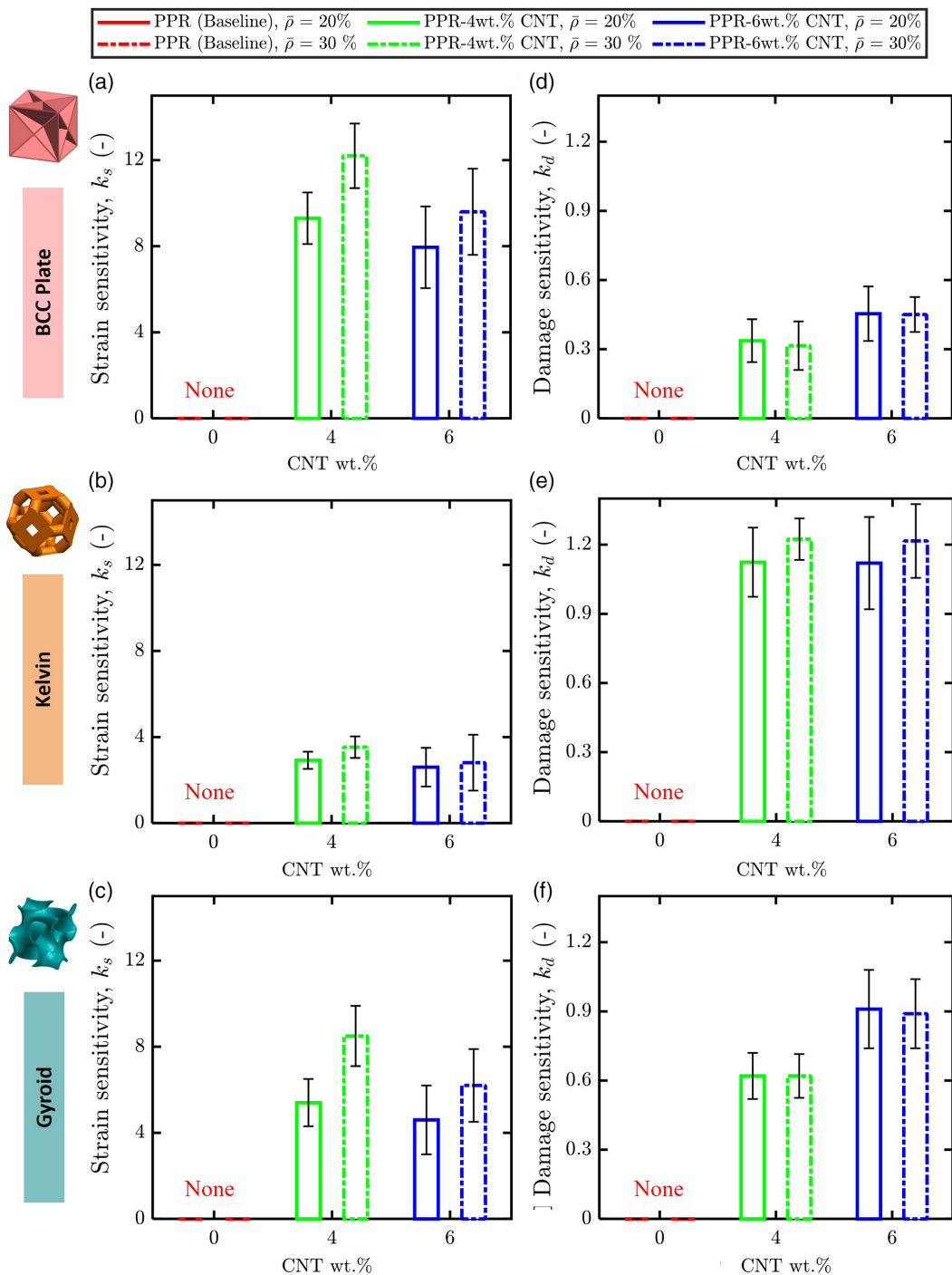


Figure 6. Piezoresistive strain resistivity and damage sensitivity of PPR/CNT cellular structures under uniaxial compression: a–c) strain sensitivity, k_s , of BCC plate, Kelvin foam, and gyroid structures of varying CNT content and relative density. d–f) Damage sensitivity, k_d , of BCC plate, Kelvin foam, and gyroid structures of varying CNT content and relative density.

predominately undergo bending deformation under compression. Unlike Kelvin foam, gyroid shell–lattices are subjected to bending as well as stretching mode of deformation. With stretching/contraction (contraction here as the structure is subjected to compressive load) as the dominant mode of deformation, gyroid–lattice structures are expected to have a smaller effect

of tensile stresses (or strains) arising from bending of members. The higher strain sensitivity, k_s , of gyroid structures (in range of 4.6–8.5) compared to Kelvin forms could be attributed to this stretching/contraction-dominated deformation behavior. Additionally, we define an average damage sensitivity given by

Table 2. Piezoresistive performance of PPR/CNT cellular structures under uniaxial compressive loading: strain sensitivity, k_s , and damage sensitivity, k_d , are listed.

Unit-cell architecture	CNT content [wt%]	Relative density [%]	Strain sensitivity, k_s (-)	Damage sensitivity, k_d (-)
BCC plate	0	20	0	0
		30	0	0
	4	20	9.3 ± 1.2	0.34 ± 0.093 ($0.121 \leq \epsilon \leq \epsilon_d$)
		30	12.2 ± 1.5	0.32 ± 0.1 ($0.136 \leq \epsilon \leq \epsilon_d$)
	6	20	8 ± 1.9	0.45 ± 0.12 ($0.114 \leq \epsilon \leq \epsilon_d$)
		30	9.6 ± 2	0.45 ± 0.08 ($0.115 \leq \epsilon \leq \epsilon_d$)
Kelvin	0	20	0	0
		30	0	0
	4	20	2.9 ± 0.4	1.12 ± 0.15 ($0.116 \leq \epsilon \leq \epsilon_d$)
		30	3.5 ± 0.5	1.22 ± 0.09 ($0.088 \leq \epsilon \leq \epsilon_d$)
	6	20	2.6 ± 0.9	1.12 ± 0.2 ($0.106 \leq \epsilon \leq \epsilon_d$)
		30	2.8 ± 1.3	1.22 ± 0.16 ($0.089 \leq \epsilon \leq \epsilon_d$)
Gyroid	0	20	0	0
		30	0	0
	4	20	5.4 ± 1.1	0.62 ± 0.1 ($0.122 \leq \epsilon \leq \epsilon_d$)
		30	8.5 ± 1.4	0.62 ± 0.095 ($0.11 \leq \epsilon \leq \epsilon_d$)
	6	20	4.6 ± 1.6	0.91 ± 0.17 ($0.103 \leq \epsilon \leq \epsilon_d$)
		30	6.2 ± 1.7	0.90 ± 0.15 ($0.111 \leq \epsilon \leq \epsilon_d$)

$$k_d = \frac{1}{R_0} \left| \frac{\Delta R}{(\epsilon_D - \epsilon_y)} \right| \quad (4)$$

where ϵ_D is the onset strain of densification of the lattice structure and ϵ_y is the initial yield strain of the lattice structure corresponding to initial peak stress. k_d evaluated in the nonlinear piezoresistive regime is shown in **Figure 6d–f** and is summarized in Table 2. Note that k_d changes with architecture, relative density, and CNT content as expected (see Table 2). The piezoresistive strain sensitivity and damage sensitivity of PPR/CNT cellular composites observed in this study are compared against all major classes of piezoresistive materials available in the literature (see **Figure 7**). It is observed that the gauge factors reported in this study for PPR/CNT lattices are comparable to those of non-AM-enabled extant materials of similar density ($<400 \text{ kg m}^{-3}$).

3.4. Mechanical Performance

All the existing low-density materials are both less strong and less stiff compared to PPR/CNT cellular composites demonstrated in this study; their strength and modulus are three orders of magnitude lower than those of the cellular structures explored in this study. For all the three architectures, an increase in CNT content results in an increase of the modulus, E (calculated by the slope of the $\sigma - \epsilon$ response in the initial linear-elastic region). PPR/CNT-6 structures show a 100% increase in modulus and an 54% increase in energy absorption with respect to PPR/CNT-0 structures of the same architecture and relative density. Among the three architectures, BCC plate-lattices show higher moduli and energy absorption, whereas Kelvin foams show the lowest moduli and energy absorption (see **Table 3**). The mechanical properties of cellular structures can be altered by changing the pore size (thereby changing the relative density).^[32] Here, by changing relative density from 20% to 30%, improved mechanical properties of cellular structures are observed. FE simulations of cellular structures of varying relative densities (from $\bar{\rho} = 5\%$ to $\bar{\rho} = 30\%$) are performed considering linear-elastic properties of PPR/CNT-6 bulk material (modulus, $E = 620 \text{ MPa}$ and Poisson's ratio = 0.4) with an applied macroscopic compressive strain of 2%. To understand the dominant deformation modes of all three architectures studied, scaling relations between relative modulus ($\bar{E} = E/E_s$, where E_s is the modulus of bulk solid $E_s = 620 \text{ MPa}$) and the relative density ($\bar{\rho}$) are obtained in the form $\bar{E} \propto (\bar{\rho})^n$. The exponent, n , signifies the dominant mode of deformation; a value of n close to 1 indicates stretching-dominated deformation behavior and a value close to 2 indicates bending-dominated behavior.^[33] It is found that for BCC plate-lattices, $\bar{E} \propto (\bar{\rho})^{1.2}$, for Kelvin foams, $\bar{E} \propto (\bar{\rho})^{2.05}$, and for gyroid structures, $\bar{E} \propto (\bar{\rho})^{1.46}$. **Figure S9**, Supporting Information, shows the relationship between \bar{E} and $\bar{\rho}$ for all three architectures. The scaling laws indicate that the Kelvin foam-lattice exhibits bending dominated-deformation behavior ($n = 2.05$) while the BCC plate ($n = 1.2$) and gyroid ($n = 1.46$) lattices show stretching-dominated behavior with BCC plate-lattice being the most stretching-dominated structure among the three. This is why the elastic modulus and strain-sensitivity factor k_s are the highest for the BCC plate-lattice, followed by the gyroid-lattice and then Kelvin-lattice. The relatively poor mechanical and piezoresistive performance of Kelvin-lattice can be attributed to its bending dominated-deformation mode (as found from FE study and reported elsewhere^[27a,27c]) and poor percolation of contacts between ligaments. Bending-dominated behavior is known to result in mechanically less efficient structures with lower stiffness and plateau stress.^[5b] Sheet-based gyroid-lattices are found to exhibit a combination of bending and stretching modes of deformation with stretching being the dominant deformation mode, offering superior mechanical performance.^[34] The better performance of the gyroid-lattice compared to Kelvin-lattice of the same relative density is due to the stretching-dominated deformation of gyroid-lattice and the absence of regions of geometric discontinuity causing reduction in stress concentrations.^[35] The reduced stress

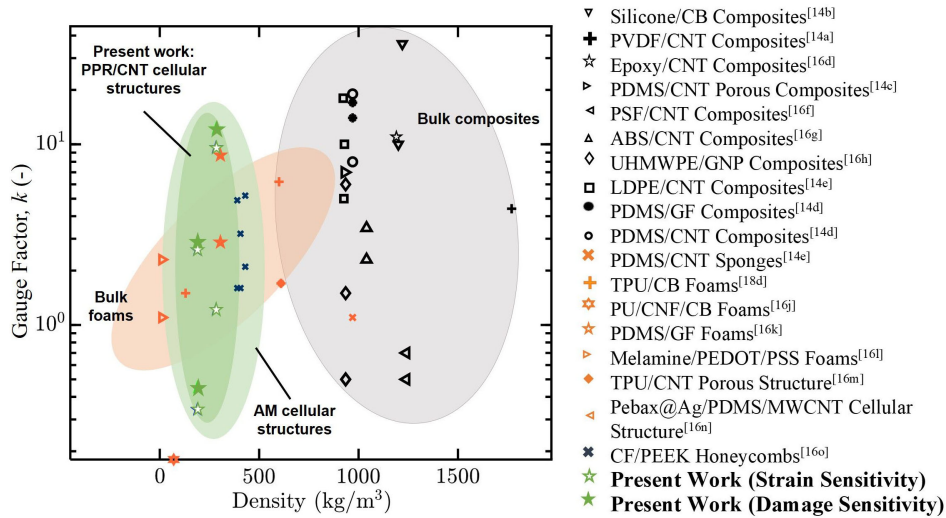


Figure 7. Comparison of gauge factors of additive manufacturing (AM)-enabled PPR/CNT cellular composites with those of extant piezoresistive materials.

Table 3. Mechanical performance of PPR/CNT cellular structures under uniaxial quasi-static compression.

Unit-cell architecture	CNT content [wt%]	Relative density [%]	Modulus [MPa]	Energy absorbed [J]	Energy absorption capacity [MJ m ⁻³]	Specific energy absorption [J g ⁻¹]	Energy absorption efficiency [%]
BCC	0	20	33.8 ± 2.3	21.1 ± 1.2	2.6 ± 0.15	13.9 ± 0.8	69.8 ± 4.1
		30	44.7 ± 2.7	29.4 ± 2.6	3.7 ± 0.33	12.9 ± 1.2	64.9 ± 5.8
	4	20	45.1 ± 2.1	24 ± 1.5	3.0 ± 0.19	15.9 ± 1	76.2 ± 4.8
		30	67 ± 3.1	30.8 ± 3.4	3.9 ± 0.43	13.6 ± 1.5	65.2 ± 7.3
	6	20	56.7 ± 4.4	30.9 ± 1.2	3.9 ± 0.15	20.5 ± 0.1	90.5 ± 3.5
		30	77.2 ± 4.1	37.9 ± 3.4	4.7 ± 0.42	16.7 ± 1.5	74 ± 6.6
Kelvin	0	20	17.2 ± 2	10.8 ± 0.9	1.34 ± 0.1	7.1 ± 0.6	35.7 ± 2.9
		30	31.5 ± 2.2	16 ± 0.9	2 ± 0.12	7.1 ± 0.4	35.3 ± 2.1
	4	20	24.2 ± 2.4	12.9 ± 0.4	1.6 ± 0.05	8.5 ± 0.27	41 ± 1.3
		30	45 ± 3.4	20.2 ± 0.9	2.5 ± 0.12	8.8 ± 0.4	42.8 ± 2
	6	20	30 ± 2.1	15.9 ± 0.8	2 ± 0.1	10.5 ± 0.5	46.6 ± 2.4
		30	63.1 ± 4.7	24.7 ± 1.8	3.1 ± 0.2	10.9 ± 0.8	48.3 ± 3.6
Gyroid	0	20	25.1 ± 1.9	13.8 ± 1.3	1.7 ± 0.16	9.1 ± 0.87	45.7 ± 4.4
		30	34.3 ± 4.5	18.1 ± 1.7	2.3 ± 0.2	8 ± 0.7	39.9 ± 3.7
	4	20	30.6 ± 2.7	15.6 ± 1.63	2 ± 0.2	10.3 ± 1.07	49.7 ± 5.2
		30	44.1 ± 3.9	20.4 ± 3.6	2.6 ± 0.45	9 ± 1.6	43.1 ± 7.5
	6	20	46.4 ± 5.1	18 ± 1.8	2.2 ± 0.2	11.9 ± 1.2	52.6 ± 5.3
		30	60.3 ± 7.1	25.6 ± 3.8	2.9 ± 0.4	10.4 ± 1.6	46 ± 6.9

concentration of the gyroid–lattice could be well understood from the von Mises stress (σ_{Mises}) distribution plot shown in **Figure 8**. Figure 8a shows the normalized von Mises stress distribution in the cellular structures (20% relative density), exhibiting the regions of localized stress concentrations in BCC plate and Kelvin–lattices. Figure 8b shows the normalized peak von Mises stress as a function of solid volume fraction (fraction of total solid volume comprised in a cellular structure, $\nu_{\text{se}} = V_e/V_s$, where V_e is the volume of selected elements and V_s is the total solid volume in the cellular structure).

Moreover, the small solid volume fraction ($\nu_{\text{se}} < 0.002\%$) of cellular structures that experience peak von Mises stresses ($\sigma_{\text{Mises,max}}$) are indicated in the plot. BCC plate– and Kelvin–lattice experience higher values of maximum von Mises stress compared to gyroid–lattice (+72% and +61% in $\sigma_{\text{Mises,max}}$, respectively). Closed-cell cellular structures composed of sheets or plates are expected to have a better mechanical performance compared to their open-cell counterparts as the interconnectivity of the cell walls of closed-cell structures provides constraint in two directions that lead to an increased

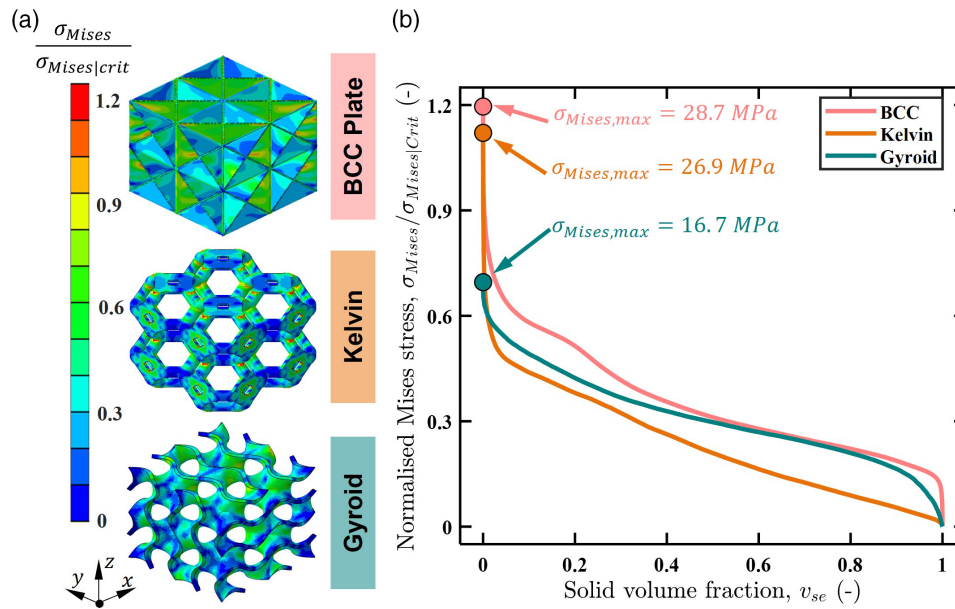


Figure 8. von Mises stress (σ_{Mises}) distribution in PPR/CNT-6 cellular composites with 20% relative density under an applied macroscopic compressive strain of 2%. a) σ_{Mises} distribution in BCC, Kelvin, and gyroid cellular structures. b) σ_{Mises} versus solid volume fraction (v_{se}) shows that higher solid volume fraction of BCC plate–lattice and gyroid–lattice experience higher σ_{Mises} compared to Kelvin–lattice.

strain energy. Compared to open-cell truss-based structures, walls of closed-cell structures undergo tensile membrane deformation with a higher volume fraction of the solid material resisting the deformation, enabling a better material utilization and an increase in mechanical performance of the structure.^[11b,11e] The strain energy density, obtained from FE studies for different cellular structures of 20% relative density with a 2% imposed macroscopic compressive strain, is analyzed to understand how effectively the material is utilized. The top row of Figure S10a, Supporting Information, shows the elements with normalized strain energy density, $\psi/\psi_s \geq 0.75$ (where ψ_s is the strain energy density of the constituent material, PPR/CNT-6 under uniform strain of 2% and ψ is the strain energy density in the cellular structure) and the bottom row shows elements with $\psi/\psi_s < 0.75$. Figure S10b, Supporting Information, shows the ψ/ψ_s distribution as a function of solid volume fraction in the structure, indicating that more solid volume fraction ($v_{se} = 24\%$) of BCC plate–lattice experiences a high strain energy density ($\psi/\psi_s \geq 0.75$) compared to Kelvin and gyroid structures. It was found that 24% of total solid volume in the BCC plate–lattice experiences higher strain energy density ($\psi/\psi_s \geq 0.75$) storing 64% of total strain energy. Compared to BCC plate–lattice, Kelvin and gyroid structures studied here have lesser fraction ($v_{se} \leq 4\%$) of the total solid volume experiencing higher strain energy density (corresponds to $\leq 22\%$ of the total strain energy). The higher strain energy density experienced by a higher solid volume fraction of BCC plate–lattice is reflected in the higher stiffness observed experimentally.

Note that the energy absorption per unit volume, Ω , is calculated from the area under the stress–strain curve up to a densification strain, $\varepsilon_D = 0.6$, as experimentally evaluated, and given by

$$W = \int_0^{\varepsilon_D} \sigma d\varepsilon \quad (5)$$

Owing to foregoing discussion, an improved mechanical performance of BCC plate–lattice compared to Kelvin– and gyroid–lattices was expected and was observed in this study (see Figure 3 and Table 3). Moreover, with increase in relative density, increase in modulus and energy absorption is observed. The highest modulus and energy absorption were observed for BCC plate–lattice of PPR/CNT-6 with 30% relative density. Other mechanical attributes such as the specific energy absorption (SEA) and energy absorption efficiency of all three lattices are also summarized in Table 3 (see Figure 3). The energy absorption per unit mass (or mass-SEA) is given by

$$\phi = \frac{1}{\rho} \int_0^{\varepsilon_D} \sigma d\varepsilon \quad (6)$$

where ρ is the density of the lattice structure. The energy absorption efficiency, η , is estimated as

$$\eta = \frac{\phi}{\phi_s} = \frac{\frac{1}{\rho} \int_0^{\varepsilon_D} \sigma(\varepsilon) d\varepsilon}{\frac{1}{\rho_s} \int_0^{\varepsilon_D} \sigma_s(\varepsilon_s) d\varepsilon} \quad (7)$$

where σ and ε are the axial compressive stress and strain experienced by the cellular structure and ε_D is the densification strain (≈ 0.6 in this study). ρ is the density of the cellular structure ($\rho = \rho_s \bar{\rho}$, where ρ_s is the density of bulk constituent material of the cellular structure) and ϕ_s is the SEA of the bulk constituent material under quasi-static compression up to ε_D (taken as 0.6).

σ_s and ϵ_s are the axial compressive stress and strain experienced by bulk solid material. The SEA of the cellular structures measured are summarized in Table 3. As the stress–strain response suggests, the SEA increases with the increase in CNT content of PPR/CNT composite lattices. The BCC plate–lattices and Kelvin structures exhibit the highest and the lowest SEA, respectively. Further, the SEA of the lattices reduces as the relative density is increased despite the increase in energy absorption, which indicates that the energy absorbed does not scale linearly with the mass when the relative density is increased from 20% to 30%. The highest SEA among the samples tested are observed for BCC plate–lattice of PPR/CNT-6 with a relative density of 20%, reporting an excellent SEA of 20.5 J g^{-1} . **Figure 9** and Table 3 show the energy absorption efficiency of the cellular structures. Note that the energy absorption efficiency of all the structures increases with increase in CNT content for a given relative density. In general, the energy absorption efficiency of all three lattice structures decrease with increase in relative

density from 20% to 30% regardless of the CNT content except for Kelvin–lattice with 4 wt% CNT content. This is because Kelvin structure with 30% relative density had a better print quality compared to structure with 20% relative density as the former had thicker struts. This could be the reason for increased energy absorption efficiency of Kelvin structure with 30% relative density. The highest energy absorption efficiency of 90.5% was observed for BCC plate–lattice of PPR/CNT-6 with a relative density of 20%. The energy absorption capacity (the energy absorbed per unit volume) are summarized in Table 3 and remarkable performance was observed for BCC plate–lattices, reporting the highest energy absorption capacity of 4.7 MJ m^{-3} .

Our nano-engineered AM-enabled lattices outperform or are comparable to a wide array of state-of-the-art cellular structures such as alloy–polymer composite lattices, alumina nanolattices, epoxy lattices, and aluminum alloy foams in terms of energy absorption as shown in **Figure 10**. Titanium alloy foams having a higher density than the PPR/CNT lattices considered in this

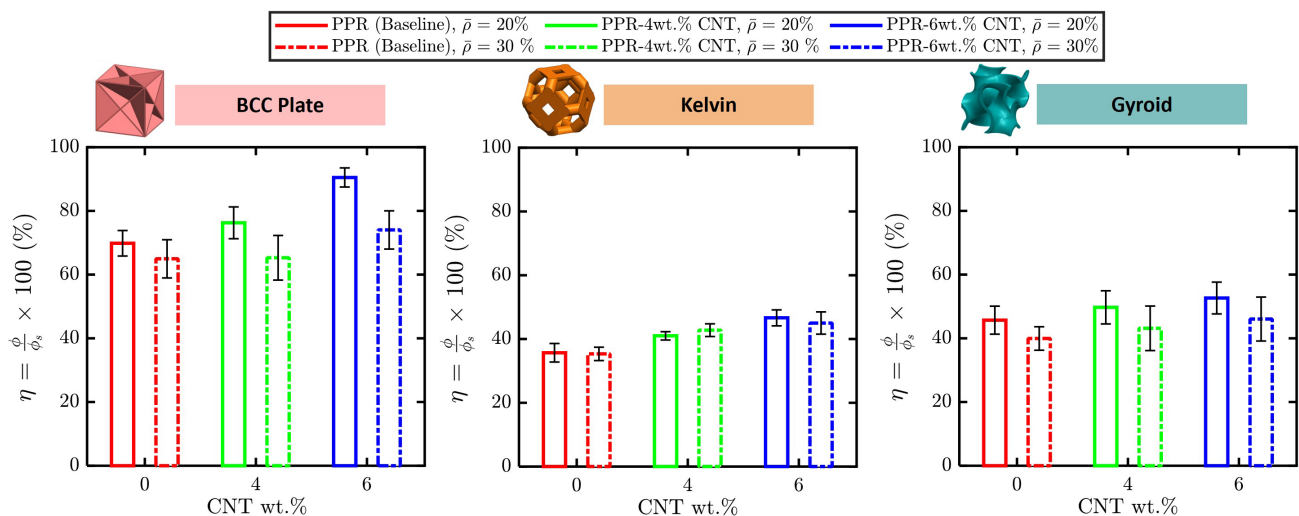


Figure 9. Energy absorption efficiency, η , of PPR/CNT cellular structures under uniaxial compression.

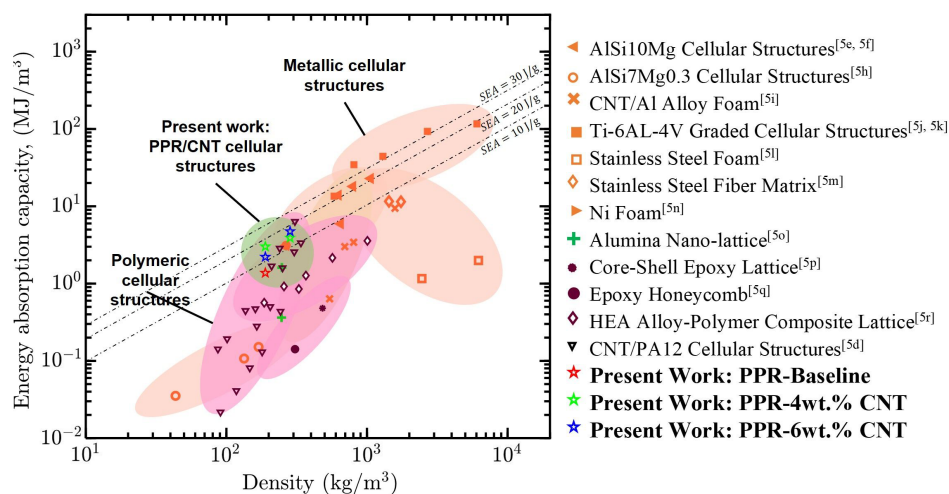


Figure 10. Comparison of energy absorption capacity of PPR/CNT cellular structures with state-of-the-art energy absorbing cellular structures.

study outperform our PPR/CNT lattices in terms of mass-specific and volume-specific energy absorption capacity. Nevertheless, titanium alloys and their manufacturing processes (especially temperatures) are cost prohibitive compared to PPR/CNT composites and lack the numerous advantages of the FFF-printing process followed in this work.

4. Conclusions

In this study, piezoresistive self-sensing and mechanical performance of FFF AM-enabled PPR/CNT 3D cellular composites is presented. Tunable strain- and damage-sensing characteristics of electrically conductive 3D lattices as a function of the architecture, relative density, and CNT content are investigated. BCC plate-lattice exhibits the highest sensitivity (strain sensitivity ranging from 8 to 12.2 and damage sensitivity ranging from 0.32 to 1.22) due to its effective material utilization and the stretching/contraction-dominated deformation behavior compared to Kelvin- and gyroid-lattices. The piezoresistive sensitivity attained for PPR/CNT cellular composites in this study are found to be comparable to other piezoresistive materials of similar density reported in the literature. Such smart lattices also showed superior and tailorable mechanical properties. BCC plate-lattice exhibits an excellent mechanical performance compared to gyroid- and Kelvin-lattices (up to 90% increase in modulus, up to 95% in energy absorption capacity compared to Kelvin-lattice of the same material and relative density; up to 50% increase in modulus, up to 64% in energy absorption capacity compared to gyroid structure of same material and relative density) due to its more stretching-dominated behavior and better material utilization attribute. The BCC plate-lattice with a CNT content of 6 wt% showed an energy absorption capacity as high as 4.7 MJ m^{-3} , which is comparable to Nickel foams of the same relative density and superior to composite truss lattices, alloy-polymer composite lattices, epoxy honeycombs, alumina lattices, and composite honeycombs of the same density. The use of low-cost FFF AM method for the manufacture of lattice structures with tunable properties can find applications in an array of fields. This study demonstrates a new route by which sensing can be engineered into 3D cellular structures and such smart cellular composites can be utilized for multifarious applications such as patient-specific orthoses, scaffolds for tissue engineering, and smart lightweight structures. The performance of these cellular structures under repetitive cyclic loading and the performance after compression are important for various applications. However, these aspects are beyond the scope of the current study and therefore suggested as a future study. The self-sensing capability introduced via the addition of electrically conductive nanofillers in this study can serve as a first comparative study that can be broadened to other nanofillers such as graphene,^[25] MXenes,^[16r] metallic nanoparticles, etc.

Supporting Information

Supporting Information is available from the Wiley Online Library or from the author.

Acknowledgements

S.K. would like to thank the University of Glasgow for the Reinvigorating Research Award (Award no. 201644-24). Authors gratefully acknowledge financial support from the ADNOC under award no. EX2016-000010. This work was supported in part by the UK Engineering and Physical Sciences Research Council (Grant no. EP/R513222/1). Authors acknowledge Dr. Pawan Verma for his support in filament fabrication.

Conflict of Interest

The authors declare no conflict of interest.

Data Availability Statement

The data that support the findings of this study are available in the supplementary material of this article.

Keywords

3D printing, carbon nanotubes, cellular composites, piezoresistive sensing, smart lattices

Received: February 17, 2022

Revised: April 19, 2022

Published online:

-
- [1] F. Forsberg, R. Mooser, M. Arnold, E. Hack, P. Wyss, *J. Struct. Biol.* **2008**, *164*, 255.
- [2] a) L. Gibson, K. Easterling, M. F. Ashby, *Proc. R. Soc. Lond. A Math. Phys. Sci.* **1981**, *377*, 99; b) S. C. Han, J. W. Lee, K. Kang, *Adv. Mater.* **2015**, *27*, 5506.
- [3] a) J. Aizenberg, J. C. Weaver, M. S. Thanawala, V. C. Sundar, D. E. Morse, P. Fratzl, *Science* **2005**, *309*, 275; b) S. Yin, H. Wang, J. Li, R. O. Ritchie, J. Xu, *J. Mech. Behav. Biomed. Mater.* **2019**, *94*, 10.
- [4] a) P. Fratzl, R. Weinkamer, *Prog. Mater. Sci.* **2007**, *52*, 1263; b) R. O. Ritchie, *Nat. Mater.* **2011**, *10*, 817.
- [5] a) E. B. Duoss, T. H. Weisgraber, K. Hearon, C. Zhu, W. Small IV, T. R. Metz, J. J. Vericella, H. D. Barth, J. D. Kuntz, R. S. Maxwell, *Adv. Funct. Mater.* **2014**, *24*, 4905; b) X. Zheng, H. Lee, T. H. Weisgraber, M. Shusteff, J. DeOtte, E. B. Duoss, J. D. Kuntz, M. M. Biener, Q. Ge, J. A. Jackson, *Science* **2014**, *344*, 1373; c) F. Wang, *J. Mech. Phys. Solids* **2018**, *114*, 303; d) S. Yuan, C. K. Chua, K. Zhou, *Adv. Mater. Technol.* **2019**, *4*, 1800419; e) L. Stanev, B. Drenchev, A. Yotov, R. Lazarova, *J. Mater. Sci. Technol.* **2014**, *22*, 44; f) I. Maskery, A. Aremu, L. Parry, R. Wildman, C. Tuck, I. Ashcroft, *Mater. Des.* **2018**, *155*, 220; g) I. Maskery, N. T. Aboulkhair, A. Aremu, C. Tuck, I. Ashcroft, *Addit. Manuf.* **2017**, *16*, 24; h) A. Jung, H. Natter, S. Diebels, E. Lach, R. Hempelmann, *Adv. Eng. Mater.* **2011**, *13*, 23; i) A. Aldoshan, S. Khanna, *Mater. Sci. Eng., A* **2017**, *689*, 17; j) S. Y. Choy, C.-N. Sun, K. F. Leong, J. Wei, *Mater. Des.* **2017**, *131*, 112; k) B. Xie, Y. Fan, T. Mu, B. Deng, *Mater. Sci. Eng., A* **2017**, *708*, 419; l) Y. Alvandi-Tabrizi, A. Rabiei, *Procedia Mater. Sci.* **2014**, *4*, 377; m) J. C. Qiao, Z. P. Xi, H. P. Tang, J. Y. Wang, J. L. Zhu, *Mater. Trans.* **2008**, *49*, 2919; n) S.-F. Fan, T. Zhang, Y. Kun, H.-J. Fang, H.-Q. Xiong, Y.-L. Dai, D.-Y. Jiang, H.-L. ZHU, *Trans. Nonferrous Met. Soc. China* **2017**, *27*, 117; o) L. R. Meza, S. Das, J. R. Greer, *Science* **2014**, *345*, 1322; p) J. Mueller, J. R. Raney, K. Shea, J. A. Lewis, *Adv. Mater.* **2018**; q) B. G. Compton, J. A. Lewis, *Adv. Mater.* **2014**, *26*, 5930;

- r) X. Zhang, J. Yao, B. Liu, J. Yan, L. Lu, Y. Li, H. Gao, X. Li, *Nano Lett.* **2018**, *18*, 4247.
- [6] J. J. Andrew, P. Verma, S. Kumar, *Mater. Des.* **2021**, *202*, 109516.
- [7] F. Alam, P. Verma, W. Mohammad, J. Teo, K. M. Varadarajan, S. Kumar, *J. Mater. Sci.* **2021**, *56*, 14070.
- [8] V. Gupta, F. Alam, P. Verma, A. M. Kannan, S. Kumar, *J. Power Sources* **2021**, *494*, 229625.
- [9] a) J. Liu, Y. Zhang, *Soft Matter* **2018**, *14*, 693; b) S. J. Yeo, M. J. Oh, P. J. Yoo, *Adv. Mater.* **2018**, 1803670; c) F. C. Campbell, in *Lightweight Materials: Understanding the Basics*, ASM International, Materials Park, OH, USA **2012**; d) J. C. Williams, E. A. Starke Jr, *Acta Mater.* **2003**, *51*, 5775; e) T. A. Schaedler, W. B. Carter, *Annu. Rev. Mater. Res.* **2016**, *46*, 187; f) T. A. Schaedler, A. J. Jacobsen, A. Torrents, A. E. Sorensen, J. Lian, J. R. Greer, L. Valdevit, W. B. Carter, *Science* **2011**, *334*, 962.
- [10] N. A. Fleck, V. S. Deshpande, M. F. Ashby, *Proc. R. Soc. A* **2010**, *466*, 2495.
- [11] a) J. Bauer, A. Schroer, R. Schwaiger, O. Kraft, *Adv. Eng. Mater.* **2016**, *18*, 1537; b) J. B. Berger, H. N. G. Wadley, R. M. McMeeking, *Nature* **2018**, *543*, 533; c) Y. Tang, Y. F. Zhao, *Struct. Multidiscip. Optim.* **2018**, *58*, 1121; d) S. Kumar, J. Ubaid, R. Abishera, A. Schiffer, V. Deshpande, *ACS Appl. Mater. Interfaces* **2019**, *11*, 42549; e) T. Tancogne-Dejean, M. Diamantopoulou, M. B. Gorji, C. Bonatti, D. Mohr, *Adv. Mater.* **2018**, *30*, 1803334.
- [12] a) L. J. Gibson, M. F. Ashby, in *Cellular solids: Structure and Properties*, Cambridge University Press, Cambridge, UK **1999**; b) D. Jang, L. R. Meza, F. Greer, J. R. Greer, *Nat. Mater.* **2013**, *12*, 893.
- [13] I. Gibson, D. W. Rosen, B. Stucker, *Additive Manufacturing Technologies: Rapid Prototyping to Direct Digital Manufacturing*, Springer, Boston, MA **2010**.
- [14] a) A. Ferreira, S. Lanceros-Mendez, *Composites, Part B* **2016**, *96*, 242; b) S. Shang, Y. Yue, X. Wang, *Rev. Sci. Instrum.* **2016**, *87*, 123910; c) Y. Wang, S. Wang, M. Li, Y. Gu, Z. Zhang, *Sens. Actuators, A* **2018**, *273*, 140; d) M. F. Arif, S. Kumar, T. K. Gupta, K. M. Varadarajan, *Composites, Part A* **2018**, *113*, 141; e) Y. Song, H. Chen, Z. Su, X. Chen, L. Miao, J. Zhang, X. Cheng, H. Zhang, *Small* **2017**, *13*, 1702091.
- [15] A. Georgopoulou, F. Clemens, *ACS Appl. Electron. Mater.* **2020**, *2*, 1826.
- [16] a) E. MacDonald, R. Wicker, *Science* **2016**, *353*, aaf2093; b) S. Jung, J. H. Kim, J. Kim, S. Choi, J. Lee, I. Park, T. Hyeon, D. H. Kim, *Adv. Mater.* **2014**, *26*, 4825; c) Y. Li, S. Luo, M. C. Yang, R. Liang, C. Zeng, *Adv. Funct. Mater.* **2016**, *26*, 2900; d) Y.-j. Kim, J. Y. Cha, H. Ham, H. Huh, D.-S. So, I. Kang, *Curr. Appl. Phys.* **2011**, *11*, S350; e) B. Herren, M. Charara, M. C. Saha, M. C. Altan, Y. Liu, *Nanomaterials* **2020**, *10*, 233; f) J. Bautista-Quijano, F. Avilés, J. Aguilar, A. Tapia, *Sens. Actuators, A* **2010**, *159*, 135; g) S. Dul, A. Pegoretti, L. Fambri, *Front. Mater.* **2020**, *7*, 12; h) T. K. Gupta, M. Choosri, K. Varadarajan, S. Kumar, *J. Mater. Sci.* **2018**, *53*, 7939; i) T. K. Gupta, S. Kumar, A. Z. Khan, K. M. Varadarajan, W. J. Cantwell, *Mater. Res. Express* **2018**, *5*, 015703; j) S. Xu, X. Li, G. Sui, R. Du, Q. Zhang, Q. Fu, *Chem. Eng. J.* **2020**, *381*, 122666; k) D. Sengupta, Y. Pei, A. G. P. Kottapalli, *ACS Appl. Mater. Interfaces* **2019**, *11*, 35201; l) Y. Ding, J. Yang, C. R. Tolle, Z. Zhu, *ACS Appl. Mater. Interfaces* **2018**, *10*, 16077; m) X. Sun, J. Sun, T. Li, S. Zheng, C. Wang, W. Tan, J. Zhang, C. Liu, T. Ma, Z. Qi, *Nano-Micro Lett.* **2019**, *11*, 1; n) Z. Ma, A. Wei, Y. Li, L. Shao, H. Zhang, X. Xiang, J. Wang, Q. Ren, S. Kang, D. Dong, *Compos. Sci. Technol.* **2021**, *203*, 108571; o) J. J. Andrew, H. Alhashmi, A. Schiffer, S. Kumar, V. S. Deshpande, *Mater. Des.* **2021**, 109863; p) C. Cai, Z. Wei, L. Deng, Y. Fu, *ACS Appl. Mater. Interfaces* **2021**, *13*, 54170; q) J. Huang, Y. Wang, J. Guo, S. Wu, H. Xie, S. Zhou, *J. Mater. Chem. A* **2022**, *10*, 3933; r) R. Qin, M. Hu, X. Li, L. Yan, C. Wu, J. Liu, H. Gao, G. Shan, W. Huang, *Nanoscale* **2020**, *12*, 17715; s) J. Zhai, Y. Zhang, C. Cui, A. Li, W. Wang, R. Guo, W. Qin, E. Ren, H. Xiao, M. Zhou, *ACS Sustainable Chem. Eng.* **2021**, *9*, 14029; t) H. Zhuo, Y. Hu, Z. Chen, X. Peng, L. Liu, Q. Luo, J. Yi, C. Liu, L. Zhong, *J. Mater. Chem. A* **2019**, *7*, 8092.
- [17] J. Chen, X. Liu, Y. Tian, W. Zhu, C. Yan, Y. Shi, L. B. Kong, H. J. Qi, K. Zhou, *Adv. Mater.* **2021**, 2102877.
- [18] a) V. Amoli, S. Y. Kim, J. S. Kim, H. Choi, J. Koo, D. H. Kim, *J. Mater. Chem. C* **2019**, *7*, 14816; b) Z. Wang, X. Guan, H. Huang, H. Wang, W. Lin, Z. Peng, *Adv. Funct. Mater.* **2019**, *29*, 1807569; c) A. Reizabal, S. Gonçalves, R. Brito-Pereira, P. Costa, C. M. Costa, L. Pérez-Alvarez, J. L. Vilas-Vilela, S. Lanceros-Méndez, *Nanoscale Adv.* **2019**, *1*, 2284; d) Y. Zhai, Y. Yu, K. Zhou, Z. Yun, W. Huang, H. Liu, Q. Xia, K. Dai, G. Zheng, C. Liu, *Chem. Eng. J.* **2020**, *382*, 122985.
- [19] A. Mora, P. Verma, S. Kumar, *Composites, Part B* **2020**, *183*, 107600.
- [20] a) S. K. Reddy, S. Kumar, K. M. Varadarajan, P. R. Marpu, T. K. Gupta, M. Choosri, *Mater. Sci. Eng., C* **2018**, *92*, 957; b) S. Kumar, T. K. Gupta, K. Varadarajan, *Composites, Part B* **2019**, *177*, 107285; c) T. Zhai, D. Li, G. Fei, H. Xia, *Composites, Part A* **2015**, *72*, 108.
- [21] Y. Yang, X. Li, M. Chu, H. Sun, J. Jin, K. Yu, Q. Wang, Q. Zhou, Y. Chen, *Sci. Adv.* **2019**, *5*, eaau9490.
- [22] a) A. Gopanna, K. P. Rajan, S. P. Thomas, M. Chavali, in *Materials for Biomedical Engineering*, Elsevier, Amsterdam, Netherlands **2019**, p. 175; b) W. Hufenbach, R. Böhm, M. Thieme, A. Winkler, E. Mäder, J. Rausch, M. Schade, *Mater. Des.* **2011**, *32*, 1468; c) M. Robert, R. Roy, B. Benmokrane, *Polym. Compos.* **2010**, *31*, 604; d) H. A. Maddah, *Am. J. Polym. Sci* **2016**, *6*, 1; e) S. Zhang, A. R. Horrocks, *Prog. Polym. Sci.* **2003**, *28*, 1517.
- [23] a) Plascore PP Honeycomb Datasheet, https://www.plascore.com/download/datasheets/honeycomb_core_documentation/PLA_PP_Honeycomb-Brochure_6-2019.pdf (accessed: October 2019); b) N. Sallih, P. Lescher, D. Bhattacharyya, *IOP Conf. Ser.: Mater. Sci. Eng.* **2018**, *370*, 012031; c) E. Lou, D. L. Hill, J. Raso, M. J. Moreau, J. K. Mahood, *Med. Biol. Eng. Comput.* **2005**, *43*, 746; d) C. Tan, H. M. Akil, *Composites, Part B* **2012**, *43*, 1433; e) The New Generation of Lightweight Core Materials - Thermhex Polypropylene Honeycomb Cores, <https://thermhhex.com/wp-content/uploads/2019/04/thermhhex-brochure-english-13112018.pdf> (accessed: October 2019); f) J. Jansz, in *Polypropylene: An A-Z Reference* (Ed: J., Karger-Kocsis) Springer Netherlands, Dordrecht **1999**, p. 643, DOI: 10.1007/978-94-011-4421-6_87.
- [24] D. Visser, D. Xue, J. L. Ronsky, J. Harder, R. F. Zernicke, *Comput. Methods Programs Biomed.* **2012**, *107*, 478.
- [25] A. Tamburrano, F. Sarasini, G. De Bellis, A. G. D'Aloia, M. S. Sarto, *Nanotechnology* **2013**, *24*, 465702.
- [26] N. Takeda, S. Minakuchi, Y. Okabe, *J. Solid Mech. Mater. Eng.* **2007**, *1*, 3.
- [27] a) R. M. Sullivan, L. J. Ghosn, B. A. Lerch, *Int. J. Solids Struct.* **2008**, *45*, 1754; b) J. A. Hawreliak, J. Lind, B. Maddox, M. Barham, M. Messner, N. Barton, B. J. Jensen, M. Kumar, *Sci. Rep.* **2016**, *6*, 28094; c) C. Ge, L. Priyadarshini, D. Cormier, L. Pan, J. Tuber, *Packag. Technol. Sci.* **2018**, *31*, 361.
- [28] a) M. F. Arif, S. Kumar, T. Shah, *Mater. Des.* **2016**, *101*, 236; b) V. R. Kumar, S. Kumar, G. Pal, T. Shah, *J. Eng. Mater. Technol.* **2016**, *138*, 041018.
- [29] a) W. Bao, S. Meguid, Z. Zhu, G. Weng, *J. Appl. Phys.* **2012**, *111*, 093726; b) A. I. Oliva-Avilés, F. Avilés, V. Sosa, *Carbon* **2011**, *49*, 2989; c) S. Gong, Z. H. Zhu, *Polymer* **2014**, *55*, 4136.
- [30] U. Deichmann, S. Schuster, J. P. Mazat, A. Cornish-Bowden, *FEBS J.* **2014**, *281*, 435.

- [31] P. Verma, J. Ubaid, K. M. Varadarajan, B. L. Wardle, S. Kumar, *ACS Appl. Mater. Interfaces* **2022**, *14*, 8361.
- [32] S. Verma, C.-K. Yang, C.-H. Lin, J. Y. Jeng, *Addit. Manuf.* **2022**, *49*, 102463.
- [33] a) M. Mohsenizadeh, F. Gasbarri, M. Munther, A. Beheshti, K. Davami, *Mater. Des.* **2018**, *139*, 521; b) J. Bauer, L. R. Meza, T. A. Schaedler, R. Schwaiger, X. Zheng, L. Valdevit, *Adv. Mater.* **2017**, *29*, 1701850.
- [34] F. Bobbert, K. Lietaert, A. A. Eftekhari, B. Pourn, S. Ahmadi, H. Weinans, A. Zadpoor, *Acta Biomater.* **2017**, *53*, 572.
- [35] D. Li, W. Liao, N. Dai, Y. M. Xie, *Materials* **2019**, *12*, 2183.